Title
Constructing a Virtual Furnace for Solid-State Thermodynamic Models

Journal
The Journal of Physical Chemistry C, 130(27)

ISSN
1932-7447

Authors
Walters, Lauren N
Jain, Anubhav
Ceder, Gerbrand

Publication Date
2026-07-09

DOI
10.1021/acs.jpcc.6c01086

Constructing a Virtual Furnace for Solid State Thermodynamic Models

Lauren N. Walters,[*,†,‡] Anubhav Jain,[†] and Gerbrand Ceder[†]

†*Division of Materials Science, Lawrence Berkeley National Laboratory, California 94720, USA*

‡*Bakar Institute of Digital Materials for the Planet, University of California Berkeley, California 94720, USA*

E-mail: LaurenWalters@lbl.gov

Abstract

Connecting 0 K density functional theory (DFT) energies to finite-temperature, finite-pressure synthesis conditions is a well-established thermodynamic formalism, yet quantified guidance on when and how accurately calibrate these results to experimental chemical potentials in practice remains sparse. In this work, we systematically benchmark a complete workflow – the virtual furnace – that constructs effective oxygen chemical potentials (μ_{O_2}) for common synthesis atmospheres (air, Ar, H_2, CO) as functions of temperature and partial pressure, and propagates quantified errors from formation enthalpies through reaction energies to critical chemical potentials. Applying this workflow to 11 binary oxides, we find that "gas-only" thermal corrections are sufficient at low temperatures and for Group II oxides across all temperatures, while solid-phase vibrational contributions become critical at elevated temperatures for transition metal oxides. We quantify this threshold through the ratio $|\Delta S_{solid}/\Delta S_{total}|$ as a practical guide for when phonon calculations are warranted. Predicted critical reduction temperatures and oxygen chemical potentials show strong agreement with industrial practice and experimental data, with typical errors of 150–250 °C for most oxides. This benchmarked workflow provides practitioners with explicit, quantified guidance for predictive modeling of phase stability and synthesis condition design.

Introduction

One tool to understand materials formation and stability are thermodynamic models mapped to experimental synthesis or processing conditions. Thermodynamic energies are often sourced from total energies (E_e) calculated by density functional theory (DFT).[1–4] A number of frameworks have been offered to adjust 0 K enthalpies computed from E_e for electronic binding and orbital errors; DFT datasets now benchmark enthalpy error thresholds for binary oxides at an average of 43 meV per formula unit or less.[5–10]

However, translating these corrected energies into experimentally meaningful synthesis

conditions and quantifying the associated errors remains poorly standardized. Energetic adjustments for solid phases at finite temperature can be included through a number of different techniques, including adjusting only entropy-dominate gaseous reference phases[11] and statistical or machine learning learning approaches.[12] More exact methods, such as introducing the temperature-dependent entropy and internal energy with vibrational Helmholtz energies (F_{vib}) from phonon calculations, require more considerable computational and time resources.[13,14] Furthermore, accurate chemical potentials to describe gaseous environments must be incorporated for reduction-oxidation active systems, as demonstrated in early ab initio atomistic thermodynamics studies of oxide surface stability.[15,16] Inspection of literature demonstrates that energetic sourcing, calibration of energies for current experimental design, and error contextualization are not comprehensively reported; for this reason, thermodynamic model construction for solid state materials formation is not standardized.

In this work, we present a clear framework for building the "virtual furnace",[15–17] *i.e.* methods for applying calculated free energies of formation to simulated experimental solid state reduction-oxidation We benchmark strategies for thermal adjustments and calculate errors for solid oxide systems. Gaseous atmospheres are scaled for effective oxygen chemical potential within different reducing environments. Our workflow provides guidance for the direct use of DFT energies to assess solid phase thermodynamic stability to aid in understanding and predicting material phase formation. To our knowledge, no single validated reference currently provides end-to-end error quantification across formation energies, reaction energies, and critical chemical potentials for a standardized set of binary oxides under realistic synthesis atmospheres.

Methods

Calculated density functional theory (DFT) energies are sourced from Materials Project[18] using pymatgen.[19] Lattice dynamics calculations were completed with the finite displacement

supercell approach using the harmonic approximation as implemented with Phonopy.[13,14] Simulation cells were constructed to have minimum lattice parameters of 9 Å. Phonon calculations were completed with the Vienna Ab Initio Simulation Package[20–23] utilizing the Projector augmented wave method,[24,25] the Perdew-Burke-Ernzerhof (PBE) functional,[26] and input parameters dictated by MPSets delivered by pymatgen.[19,27] Experimental data, including enthalpies, entropies, heat capacities, and parameters for the Shomate equations were sourced primarily from the National Institute for Standards and Technology's (NIST) JANAF Thermochemical Tables.[28,29]

To calculate thermodynamic quantities for gases, we used variations of the Shomate equations.[28,30] For oxygen, these are:

$$H^\circ - H^\circ_{298.15} = A \cdot t + B \cdot t^2/2 + C \cdot t^3/3 + D \cdot t^4/4 - E/t + F - H \tag{1}$$

$$S^\circ = A \cdot \ln(t) + B \cdot t + C \cdot t^2/2 + D \cdot t^3/3 - E/(2 \cdot t^2) + G \tag{2}$$

where C_p° is the heat capacity at temperature T in Kelvin, H° is the standard enthalpy at temperature T, S° is the standard entropy at temperature T, t=$T/(1000\,\mathrm{K})$ temperature T, A, B, C, D, E, F, G, and H are empirical fit factors sourced from the NIST-Janaf Thermochemical Tables,[28] and are reproduced in Table S1-Table S5. Shomate equation values must be referenced to a 298 K reference state. When starting from 0 K DFT energies, this adjustment can be made using experimental enthalpy and entropy differences between 0 K and 298 K, or from phonon calculations reporting vibrational energy combined with translational and rotational contributions. In this work, experimental thermochemical data were used for this correction.[31]

Results

Accurate Energetic Models for the Solid State

The formation free energy of a phase (M_xO_y) at T ($\Delta_f G_T$) contains temperature-dependent enthalpic and entropic contributions according to

$$\Delta_f G_T = \Delta_f H_T - T\Delta S_T \,, \tag{3}$$

where $\Delta_f H_T$ is the formation enthalpy and ΔS_T is the formation entropy of M_xO_y at temperature T. When utilizing DFT to find accurate approximations for formation free energies, vibrational enthalpy $\Delta E^{CALC}_{T,vib}(M_xO_y)$ and entropy $\Delta S^{CALC}_{T,vib}(M_xO_y)$ obtained from the phonon density of states are often used to adjust calculated 0 K enthalpies $\Delta_f H^{GGA}_{0K}$ to finite-temperature. While, in principle, the entropy of O_2 gas can also be calculated, it is common to use experimentally obtained values. Thus, Equation 3 can be re-composed to contain terms directly calculable terms by DFT:

$$\begin{aligned}\Delta_f G^{CALC}_T(M_xO_y) \approx & \Delta E^{CALC}_e(M_xO_y) + \Delta E^{CALC}_{T,vib}(M_xO_y) \\ & - T(S^{CALC}_{T,vib}(M_xO_y) - xS^{CALC}_{T,vib}(A) - \frac{y}{2}S^{EXP}_T(O_2)) \\ \approx & \Delta E^{CALC}_e(M_xO_y) - \Delta F^{CALC}_{T,vib}(solids) - \frac{y}{2}TS^{EXP}_T(O_2)\,,\end{aligned} \tag{4}$$

where $F^{CALC}_{T,vib}$ is the vibrational Helmholtz energy found from $E^{CALC}_{T,vib} - TS^{CALC}_{T,vib}$ for each phase, and E_e is the total energy used to approximate H_{0K} and which is generally adjusted with systematic or machine-learned corrections.[5–10] While there are numerous reports of utilizing phonon-derived thermodynamic quantities to model $\Delta_f G^{CALC}_T$ [7,13–16,31], calculation of vibrational energies is not always performed due to the high resource costs.

Table 1: Reference table for thermodynamic models of energetic contributions to reaction energies of phase M_xO_y. Terms are presented as $\Delta E^{\text{energetic source}}_{\text{temperature (temperature adjustment terms)}}$. Comparison of different thermodynamic models for binary oxides are presented in Figure 1.

Thermodynamic Term	**Gas Phase Thermal Correction (Gas-Only Model)**	**Gas and Solid Phases Thermal Correction (Gas-Solid Model)**	**Modified Energetic Source**
Enthalpy ($\Delta_f H$)	$\Delta_f H^{MP-GGA}_{0K}$	$\Delta_f H^{MP-GGA}_{T(gas+solid)}$	$\Delta_f H^{GGA}_{0K}$
Entropy (ΔS)	$\Delta S^{EXP}_{T(gas)}$	$\Delta S^{EXP,MP-GGA}_{T(gas+solid)}$	-
Free Energy ($\Delta_f G$)	$\Delta_f G^{MP-GGA}_{T(gas)}$	$\Delta_f G^{MP-GGA}_{T(gas+solid)}$	$\Delta_f G^{SISSO}_{T}$

Table 1 shows a handful of models, each with different associated resource costs, that can be leveraged to approximate (temperature-dependent) enthalpy $\Delta_f H$, entropy ΔS, and free energy $\Delta_f G$. The model in the first column use T-independent DFT-energies and T-dependence of $\Delta_f G$ accounted for by the entropy of the O_2 gas. This approximation is often used because the O_2 entropy dominates the T-dependence of $\Delta_f G$ in oxidation/reduction reactions, and no calculation of phonon spectra is required. In the middle column, finite temperature terms arising from solid phase vibrations are included through phonon calculations of the participating solid phases. In the final column, we present a commonly used model which takes ground state DFT energies with no additional adjustments, and approximates the finite-temperature free energy using SISSO (Sure Independence Screening and Sparsifying Operator), a descriptor model trained on experimental entropic contributions to the free energy for a broad range of oxides.[12] This model was developed and validated with binary and ternary oxides, making it directly applicable to the oxide systems studied here, and its low computational cost makes it a practical baseline for comparison against a phonon-based approach.

In Figure 1 we present the difference between thermodynamic quantities calculated by models in Table 1, and their associated reference experimental data at 298 K. $\Delta_f H$, ΔS, and $\Delta_f G$ models, sourced from density functional theory MP-GGA energies,[18] are fit by adjusting for temperature with gas phases only included, or with gas and solid phases. For additional comparison, models with direct energetic corrections are also shown: for enthalpy,

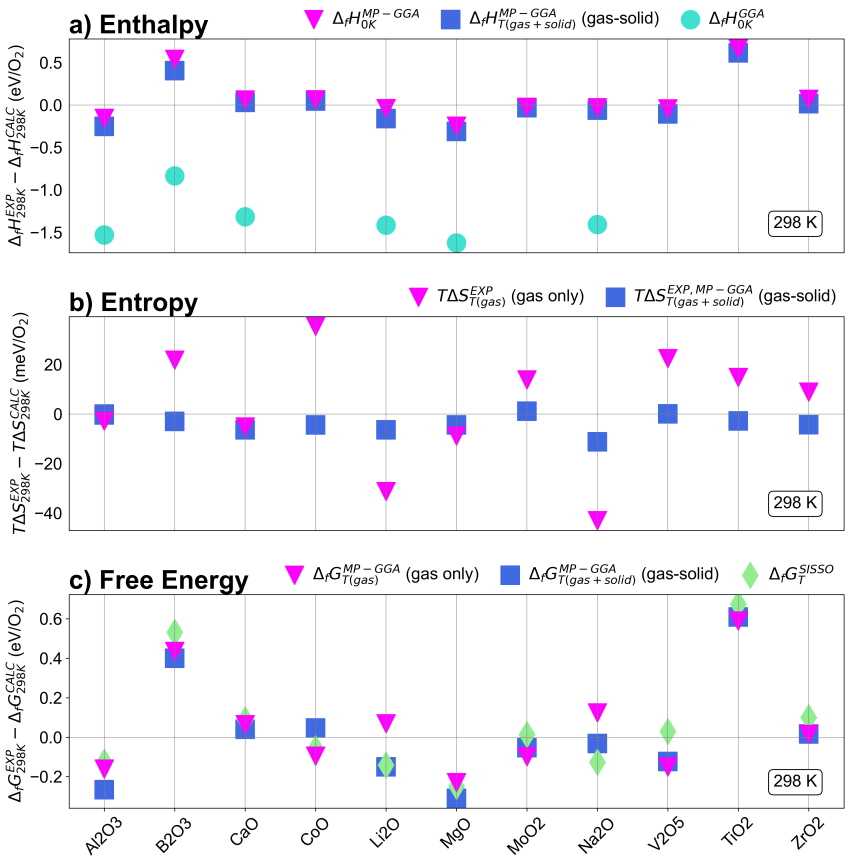

Figure 1: Comparisons of strategies to adjust DFT-energies for errors and finite temperatures against experimental values from NIST-Janaf[28] at 298 K for binary oxides. All DFT data is sourced from the materials project and fit adjusted with systematic correction schema as described in the Methods except where noted. (a) In pink triangles are the enthalpies from the Materials Project without associated energy corrections, but without any temperature adjustment. Blue squares are the same 0 K enthalpy but with finite T-adjustment for solid and gas phases. Teal circles are the uncorrected GGA values. (b) Results for $T\Delta S_T$ differences at 298 K between experimental values and those calculated with the gas-only model $\Delta S_{T(gas)}^{EXP}$ (pink triangles) and the gas-solid model $\Delta S_{T(gas+solid)}^{EXP,GGA}$ (blue squares). (c) Results for numerical difference between $\Delta_f G_{298K}^{EXP}$ and those calculated with DFT-GGA from Materials Project for binary oxides adjusted by the gas-only model $\Delta_f G_{T(gas)}^{MP-GGA}$ (pink triangles), the gas-solid model $\Delta_f G_{T(gas+solid)}^{MP-GGA}$ (blue squares), and estimated by SISSO $\Delta_f G_T^{SISSO}$ (green diamonds).[12] Consistent symbol shapes and colors across panels (a-c) denote similar thermodynamic models, allowing visual comparison of enthalpy, entropy, and free energy errors for each approach.

enthalpic corrections[32,33] are excluded in $\Delta_f H_{0K}^{GGA}$ data, and for free energy, the SISSO method temperature fitting is employed in ΔG_T^{SISSO} data.[12]

Figure 1a shows the differences between the experimental $\Delta_f H$ and those calculated with the gas-only ($\Delta_f H_{0K}^{MP-GGA}$) and gas-solid ($\Delta_f H_{T(gas+solid)}^{MP-GGA}$) models for T-dependence added to the MP-corrected GGA energies. The uncorrected GGA energies $\Delta_f H_{0K}^{GGA}$ are also shown. All DFT values are calculated with the GGA functional by the Materials Project and adjusted with systematic composition and oxidation state energetic corrections for DFT-GGA/DFT-GGA+U (implemented by the *MaterialsProject2020Compatibility* class).[32,33] With no additional adjustment, calculated $\Delta_f H_{0K}^{GGA}$ deviate by $> 1\,\mathrm{eV/atom}$ for a number of different phases. In particular, the difference between MgO experimental and calculated, uncorrected enthalpies is -1.62 $\mathrm{eV/O_2}$. Due to the significant differences in experimental and calculated values, correction schema have been developed that drastically improve calculated DFT enthalpies. However, we note that many the systematic energy corrections, including those employed by Materials Project, implicitly includes the zero point energy (ZPE)[5] as it is embedded in the experimental 0 K enthalpy. This value is also included in the gas-solid model with the vibrational enthalpy term $\Delta E_{vib,298K}$ obtained from the phonon calculations. Therefore, the ZPE is double counted in the gas-solid model when applied to $\Delta_f H^{CALC}$ already adjusted for the ZPE at 0 K. Figures S1 to S5 demonstrate that MP-GGA $\Delta_f H_{0K,ALL}^{MP-GGA}$ are offset from experimental values by about 85 meV/O at 298 K. This is roughly equivalent to the average ΔZPE calculated for oxides from reference states with phonon calculations in this study (see ZPEs reported in Table S10). Therefore, to avoid double counting the zero point energy, we propose an adjustment of 85 meV/O when utilizing the Materials Project GGA/GGA+U-sourced (MP-GGA) adjusted enthalpies where and adding phonon-based vibrational effects.

Enthalpies at 298 K obtained with various schema and referenced to the experimental value are shown in Figure 1a. Enthalpies at 0 K without solid phase finite-T corrections $\Delta_f H_{0K}^{MP-GGA}$ are within $< 664\,\mathrm{meV/O_2}$ of all experimental values, and on average deviate by

177 meV/O_2. Inclusion of the solid phase T-dependent terms $\Delta_f H^{MP-GGA}_{298K,ALL}$, after adjustments to prevent ΔZPE double-counting, demonstrates slightly higher deviation from experiment, at an average of 185 meV/O_2, however, the maximum deviation is lowered to 614 meV/O_2. Some solids show generally poor agreement with experiment, notably for B_2O_3 and TiO_2. Explanations for these errors from previous studies center on the exclusion of key physics in high throughput calculations for both materials: van der Waals corrections for the B reference and boroxide,[34] and a +U self-interaction correction for TiO_2 for accurate charge transfer and orbital occupancy between Ti and O.[35,36]

Figure 1b shows the difference between experimental and calculated entropies ($T\Delta S_{298K}$) for 11 oxides at T =298 K, p =1 atm (standard state). The gas-only $\Delta S^{EXP}_{T(gas)}$ (pink circles) and, gas and solid phase correction $\Delta S^{EXP,MP-GGA}_{T(gas+solid)}$ (blue squares) models of entropy are plotted. With the gas-solid model, the difference between experimental and calculated values is less than 12 meV/O_2 for every oxide. In the gas-only model, the average difference is 19 meV/O_2, with the largest difference being 43 meV/O_2. The largest errors are associated with CoO (35 meV/O_2), Li_2O (-31 meV/O_2), and Na_2O (-43 meV/O_2). However, these entropy errors are still an order of magnitude less than the average error associated with enthalpy calculations for all models included in this work. Note that errors associated with the enthalpic and entropic models included in this work become generally larger at higher temperatures.

The ratio of entropy change $|\Delta S_{\text{solid}}/\Delta S_{\text{total}}|$, reported in Table S7 for all eleven oxides at 298 K and 700 K, provides a practical metric for assessing when solid-phase contributions must be included in thermodynamic models. At 298 K, the ratio of entropy change spans from less than 2% for Al_2O_3 to 29% for CoO, demonstrating that the gas-phase entropy of O_2 dominates ΔS_{total} for many oxides at standard conditions, and the gas-only model would likely be sufficient. However, at elevated temperatures, the ratio of entropy change becomes increasingly significant for transition metal oxides: CoO reaches 83% and V_2O_5 increases from 17% to 38% by 700 K. Conversely, Group II oxides such as MgO and CaO

have the ratio of entropy change remain below 13% across both temperatures, confirming that the gas-only model is adequate for these systems even at high temperatures. We propose $|\Delta S_{\text{solid}}/\Delta S_{\text{total}}| \approx 10\%$ as a practical threshold: below this value, solid-phase contributions from phonon calculations are unlikely to meaningfully improve agreement with experiment, and the high computational expense of utilizing the gas-solid model could be weighed.

In Figure 1c, we present the difference in experimental and calculated $\Delta_f G_T$ at 298 K. Three models for temperature-dependence are included: the gas-only $\Delta_f G^{MP-GGA}_{T(gas)}$, the value with gas and solid phases-included $\Delta_f G^{MP-GGA}_{T(gas+solid)}$, and the SISSO method $\Delta_f G^{SISSO}_T$ (teal triangles)[12] models. The average $\Delta_f G$ difference when solid phase entropy is included is 0.186 eV/O_2. The gas-only model yielded slightly lower disparity from experimental $\Delta_f G_T$ of 0.185 eV/O_2 at 298 K, due to an overestimated $F_{T,vib}$. Notable outliers are B_2O_3 and TiO_2, whose overestimated $\Delta_f G^{CALC}_{298K}$s are attributed to severely overestimated $\Delta_f H^{CALC}_{298K}$ as shown in (a). The largest $\Delta_f G^{EXP} - \Delta_f G^{MP-GGA}$ found is for TiO_2, at 0.59 eV/O_2 (gas-solid model) and 0.61 eV/O_2 (gas-only model). For most phases, both the gas-solid and gas-only models overestimate (are more negative than) the experimental value. In Figure 1c, we also show the $\Delta_f G^{SISSO}_T$ difference from experiment calculated with the SISSO method. $\Delta_f G^{SISSO}_T$ values are closer to experiment than the other calculated methods at an average difference of 0.194 eV/O_2. Seven out of eleven oxides show a difference from experiment less than 0.2 eV/O_2. However, we also note that $\Delta_f G^{SISSO}_T$s are not systematically over or under approximated. One important example is MoO_2, where $\Delta_f G^{MP-GGA}_T$ are approximately -50 to -100 meV/O_2 more negative (stable) than experiment, and the $\Delta_f G^{SISSO}_T$ is over 23 meV/O_2 less negative (less stable).

We attribute the majority of the deviation of $\Delta_f G^{CALC}_T$ from experimental values to the enthalpy error in DFT-GGA energies. Figure 1a, Table S6 and Table S8 show the enthalpy and free energy values calculated with different temperature dependence models, compared to experiment, for specific oxide phases. Regardless of the correction schema, the difference between experimental and calculated free energy of formation is very similar to

the error in the enthalpy. For example, $\Delta_f H^{298K}_{EXP} - \Delta_f H^{MP-GGA}_{298K}$ for Al_2O_3 is -0.377 eV/O_2 for solid phases included ($\Delta_f H^{MP-GGA}_{T(gas+solid)}$) and -0.235 eV/$O_2$ without solid phase vibrational effects included ($\Delta_f H^{MP-GGA}_{0K}$), respectively. If we compare these values to the errors on the free energy of formation $\Delta_f G^{EXP}_{298K} - \Delta_f G^{MP-GGA}_{298K}$ for Al_2O_3, -0.399 eV/O_2 (gas-solid) and -0.242 eV/O_2 (gas-only model), this difference is about 5% or less for both fit schema. This highlights the importance of accurate enthalpy sourcing from DFT, either through the choice of functional or other empirical adjustments. We note other post-calculation methods beyond those employed here have been proposed, such as defining solid oxygen reference phases or developing additional bonding corrections,[7,10] however, reported errors are still on the order of 0.1 eV/O_2. Errors in $\Delta_f G^{CALC}_T$ therefore arise from several compounding sources: (1) the choice of DFT functional and associated correction schema for 0 K enthalpies, where TiO_2 and B_2O_3 show deviations exceeding 0.5 eV/O_2 (Figure 1a); (2) approximations inherent to the quasi-harmonic phonon treatment of vibrational free energies; (3) the use of experimental rather than calculated O_2 entropy; and (4) the implicit reference state choices embedded in the MP compatibility corrections, including the treatment of ZPE described above.

Virtual furnace for oxygen

Construction of a "virtual furnace", a model for predicting materials formation and stability during heating, necessitates proper accounting for experimental conditions. In the previous section, we discussed methods to modify DFT reaction energies for finite temperatures. Here and in the following section, we consider partial pressure (p) and chemical potential (μ) calibration of the gaseous reduction or oxidation agent(s).

In both open-air box furnaces and controlled atmospheres heating under inert gases like argon and nitrogen, commonly used in solid state synthesis or for the reduction of oxides, the redox active agent is often oxygen gas. Oxidation of metal M to an oxide $M_x O_y$ is described by

$$xM + \frac{y}{2}O_2 \rightarrow M_xO_y \qquad (\Delta G_{rxn})\,, \tag{5}$$

where x,y are stoichiometric coefficients, ΔG_{rxn} is the reaction free energy constructed from $\Delta_f G_T$s, and the reverse reaction defines reduction. The thermodynamic equilibrium (K_p) depends on the oxygen partial pressure (p_{O_2}) and ΔG_{rxn}:

$$K_p = \frac{1}{p_{O_2,eq}} = exp(-\frac{\Delta G_{rxn}}{RT}) \,, \tag{6}$$

where R is the ideal gas constant and T is the temperature in Kelvin. If the realized (experimental) partial pressure $p_{O_2,exp.}$ is greater than the equilibrium $p_{O_2,eq.}$, then oxidation is thermodynamically predicted to occur. If an oxide is initially present, reduction is predicted for $p_{O_2,exp.} < p_{O_2,eq.}$.

There are a number of different strategies to find or predict the experimental p_{O_2} in a furnace. These include direct measurement with gas partial pressure sensors, benchmarking reduction-oxidation of known standards, and estimation from the grade of the supplied gas. For open air and box-type furnaces, p_{O2} is presumed to be the oxygen partial pressure in air at sea level at 0.21 atm. For furnaces with controlled, inert atmospheres or under vacuum (*e.g.* tube furnaces with argon), some level of oxygen impurity may be expected. We estimate p_{O2} under argon as the commonly reported impurity content for high purity purchased argon at 1 ppm by volume, or approximately 10^{-6} atm. In practice, p_{O2} can vary in sealed furnaces due to leakage and should be confirmed with gas sensors for accuracy if possible. It is important to note that minimum bounds for p_{O2} can be approximated in furnaces; in a 1 L furnace with 1 molecule of O_2, $p_{O2} = 4 \times 10^{-25}$ atm at room temperature.

Virtual furnace for other gases

The virtual furnace can also be constructed for heating in alternative atmospheres including reducing agents, *e.g.* $H_{2(g)}$, $C_{(s)}$, $CO_{(g)}$. As is well established in the field of metallurgy, these reducing agents correspond to an equivalent partial pressure.

Reduction with Hydrogen Gas

The direct oxidation of element M by water may be written as

$$M_x + yH_2O \rightarrow M_xO_y + yH_2\,, \tag{7}$$

where the reverse reaction represents the reduction of the oxide by hydrogen gas. In this case, the relevant parameter that controls oxidation/reduction is $\frac{p_{H_2O}}{p_{H_2}}$, and indeed, is the quantity that is typically used to quantify a H_2/H_2O gas mixture. Reaction equilibria should therefore be normalized per mole water or per mole hydrogen. Each $\frac{p_{H_2O}}{p_{H_2}}$ (P_{HH}) corresponds to an equivalent partial pressure through the temperature-dictated equilibrium

$$\frac{p_{H_2O}}{p_{H_2}} = K_p \cdot p_{O_2}^{0.5}\,, \tag{8}$$

where K_p is defined as $-RT\ln(\Delta G_{rxn})$ for $H_2 + \frac{1}{2}O_2 \rightleftharpoons H_2O$. Because of the flammable nature of H_2, its content is usually limited to 1 or 2% in an inert carrier gas.

Multiple possible strategies can be used to record P_{HH}. The most accurate method is real time monitoring of $H_{2(g)}$, $O_{2(g)}$, and $H_2O_{(g)}$ with gas sensors. *A prior* prediction of the approximate P_{HH} is possible by estimating hydrogen and water vapor content. The most reducing P_{HH} occurs when only a single molecule of H_2O will be created before flowing out of the system. For a 1 L tube furnace with 8.17×10^{-4} moles of H_2 (*e.g.* 2 % by volume) present alongside 1 molecule (6.022×10^{-23} moles) water gives a minimum $\frac{p_{H_2O}}{p_{H_2}} = 3.01 \times 10^{-21}$. A more realistic P_{HH} is found to be 5×10^{-5}, calculated from a 2% volume H_2 and a H_2O impurity level of 1ppm (1×10^{-6} atm).

Reduction with Solid Carbon

A similar methodology is leveraged for modeling reduction by solid carbon or carbon monoxide. In this case, solid carbon is oxidized in inert atmosphere through consuming oxygen from an

oxide, resulting in the release of carbon monoxide or dioxide as

$$M_xO_y + \frac{y}{2}C \rightarrow M_x + \frac{y}{2}CO_2\,,\; M_xO_y + yC \rightarrow M_x + yCO\,, \tag{9}$$

where $CO_{2(g)}$ is favored below $\approx 700\,^{\circ}C$, and $CO_{(g)}$ is created above $\approx 700\,^{\circ}C$. The initial creation of $CO_{(g)}$ leads to a secondary possible redox reaction via

$$M_x + yCO_2 \rightarrow M_xO_y + yCO\,. \tag{10}$$

In the remainder of this section, we will address only high temperature reactions $> 700\,^{\circ}C$.

The gaseous equilibrium for carbothermal reduction is defined by

$$CO + 0.5O_2 \rightarrow CO_2\,. \tag{11}$$

Thus, the critical gaseous equilibrium parameter is $\frac{p_{CO2}}{p_{CO}}$ (P_{CC}), which is equivalent to the effective p_{O_2} through the equilibrium in Equation 11:

$$\frac{p_{CO2}}{p_{CO}} = K_p \cdot p_{O2}^{0.5}\,. \tag{12}$$

Operating P_{CC} can be established in a number of different ways: approximated as the temperature defined equilibrium of Equation 11, set to flowing gas input concentrations, monitored partial pressures with gas sensors, or approximated with a simple conversion rate model. As-purchased ultra pure grade Ar generally contains CO_2:CO ratios at 0.5 to 1 ppm each, thus defining the P_{CC} with no additional carbon source present as 1. In many works, carbothermal reduction is carried out with flowing CO and CO_2 gas mixtures, thus allowing for precise control of P_{CC}.[37] As an example a 20%CO/80%Ar with assumed impurities of 0.5ppm CO_2 impurity (delivered by as-purchased ultra pure Ar), yielding $p_{CO} = 0.2\,\text{atm}$, $p_{CO2} = 5 \times 10^{-7}\,\text{atm}$, and a $P_{CC} = 2.5 \times 10^{-6}$.

Application of the Virtual Furnace to Binary Oxides

One standard model for understanding equilibrium reduction-oxidation is the enumeration and calculation of possible reactions within the Ellingham diagram construction.[7,38,39] In Figure 2, we present Ellingham diagrams for a set of binary oxides with various approximations of the reaction free energy. The left scale on the vertical axes show the reaction free energy normalized per mole O_2 reacted. The right axes are nomographic scales depicted to calculate the equilibrium p_{O_2} at each pressure. Light gray lines are overlaid to guide finding oxygen equilibrium partial pressure at different temperatures. Within the Ellingham diagram framework, partial pressures at a given temperature above the reaction energy line drive the forward oxidation reaction and lower partial pressures favor reduction.

Figure 2a presents reaction free energies sourced from experimental data using different T-dependence models. Solid, black lines (labeled $\Delta_f G^{EXP}_{rxn}$) show reaction equilibrium lines generated with free energies of formation ($\Delta_f G^{EXP}_{T}$) from the NIST-JANAF Thermochemical Tables.[28] The blue, dashed lines depict the same reaction equilibria, but with entropic contributions from gaseous terms only ($\Delta_f H^{EXP}_{T} - T\Delta S^{EXP}_{T(gas)}$). Magenta, dotted lines show experimentally sourced reaction energies that neglect temperature dependence for all solid phases (experimental-gas-only model) ($\Delta_f H^{EXP}_{0K} - T\Delta S^{EXP}_{T(gas)}$). As such, the enthalpy of formation at 0 K is used for all temperatures.[28] Consistent with previously reported Ellingham diagrams,[38] reaction energies trend up (lower oxygen partial pressure, less negative reaction energy) with higher temperature due to the higher negative reaction entropy of metal-oxidation reactions. When comparing the different temperature adjustment models, reaction free energies calculated with entropies only from gas phases (experimental-gas-only models) become less negative, making the oxide slightly less stable. In other words, inclusion of solid phase entropies decreases reaction energy (reaction energy is more negative, oxidation is more favorable) at high temperature. CoO and TiO_2, B_2O_3, and V_2O_5 show some of the largest deviations between experimental reaction energies, and those that include temperature-dependence from O_2 only (gas-only model). This can be understood by the

large solid phase entropy contribution for the formation of these oxides. For instance, the ratio for $\frac{\Delta S_{T,solids}}{\Delta S_{T(gas+solid)}}$ is 0.6 at 700 K for CoO. In other words, solid phases contribute $\approx$60% of the reaction entropy. On the other hand, CaO and MgO exhibit near overlap between the reaction energy calculated with $\Delta_f G^{EXP}_{rxn}$ and from $\Delta_f H^{EXP}_T - T\Delta S^{EXP}_{T(gas)}$ (gaseous entropies only) equilibria, demonstrating that the relative contribution of entropy from solid phases is a smaller energetic contribution ($\frac{\Delta S_{T,solids}}{\Delta S_{T(gas+solid)}} < 0.1$ at all temperatures). Li_2O and Na_2O are the only oxides in this collection whose reaction equilibria are more negative with only gas phase entropy included in the temperature adjustment ($\Delta S_T : \Delta S^{EXP}_{T(gas)}$). This can be explained by the relative contribution to the entropy from solid phases being quite small $\sum S_{T,\,solid\,products} - \sum S_{T,\,solid\,reactants} \approx 0.1\,\mathrm{eV/atom}$.

In Figure 2b, we present and compare DFT-calculated reaction free energies for the same set of binary oxides. As in Figure 2a, reaction equilibria calculated with free energies of formation from experiment are labeled as $\Delta_f G^{EXP}_{rxn}$ and shown with solid black lines. The other two reaction equilibria lines are calculated with 0 K enthalpies from MP-GGA energies. The teal dashed lines depict reaction energies adjusted for temperature with solid phase vibrational contributions included (gas-solid model) as $\Delta_f H^{CALC}_{T(gas+solid)} - T\Delta S^{EXP,CALC}_{T(gas+solid)}$. In the orange dotted line labeled $\Delta_f H^{CALC}_{0K} - T\Delta S^{EXP}_{T(gas)}$, no vibrational energies from phonon calculations are considered, and thus solid phase contributions to temperature are omitted (gas-only model). In general, we find good agreement between DFT-calculated and experimental reaction energies for the considered oxides. The gas-only model reaction equilibria, which does not include solid phase temperature models, show a steeper slope from a larger energy change with temperature than the gas-solid model equilibria. Both sets of MP-GGA calculated reaction energies largely preserve the reduction series for the oxides. For nearly all oxides, the reaction energy divergence from experiment ($\Delta_f G^{EXP}_{rxn}$) increases with rising temperature. The reaction energy of a handful of oxides, B_2O_3 and TiO_2, deviates by more than 10% from the experimental value at low temperature. Inaccurate 0 K enthalpies for TiO_2 and B_2O_3 are associated with chosen electronic structure methods. Previous DFT studies include *ad hoc*

+U correlation for TiO_2[35,36] and consideration of van der Waals corrections for elemental B,[34] which are not used for this work. Divergence of reaction equilibria at higher temperature is associated with small differences in calculated and experimental solid phase entropies (shown in Table S9). Beyond solid phase entropy errors, reaction energy errors at all temperatures inherit inaccuracies from the 0 K enthalpy for specific systems such as TiO_2 and B_2O_3 (Figure 2b), and at elevated temperatures, from uncertainties in Shomate equation fits used to interpolate experimental thermochemical data, which compound with growing solid-phase entropy errors for transition metal oxides such as CoO (see Table S9). For instance, while the inclusion of solid phase entropies in the gas-solid temperature adjustment model helps the calculated CoO equilibria come closer to experimental values, the calculated S_{300K} is 27.9114 J/K/mol for elemental Co versus 30.221 J/K/mol from NIST-JANAF Tables.[28]

Assessing Critical Reduction Chemical Potential

To better understand reduction and oxidation in specific furnace settings, we calculate the effective μ_O at which a metal oxide reduces in specific furnace conditions. In Figure 3, we present the reducing μ_O (critical reduction point) for a collection of binary and ternary/quaternary oxides in air, argon, 2 % H_2 gas, and in excess solid carbon. A collection of 46 common binary oxides are considered (see Table S11 for full list), for which we use $\Delta_f G_T^{EXP}$ sourced from experimental databases.[28,29] In addition, we also evaluate a handful of Li battery cathode materials for which we use enthalpies from DFT corrected by gas phase entropies only: $LiCoO_2$, $LiMn_2O_4$, $LiFePO_4$, Li_2VO_3, and $Li_4Mn_3Co_2Ni_3O_{16}$.[40] The critical reduction point is defined as the temperature and associated effective oxygen chemical potential when reduction from oxide to elements becomes thermodynamically favored. Only materials with a predicted reduction point in the chemical potential range are shown. The stability of all 46 oxides was cross-checked against competing hydroxide, hydride, carbonate, and carbide formation (see Table S12); in all cases, oxide reduction to elements occurs at a lower temperature than possible competing phase formation.

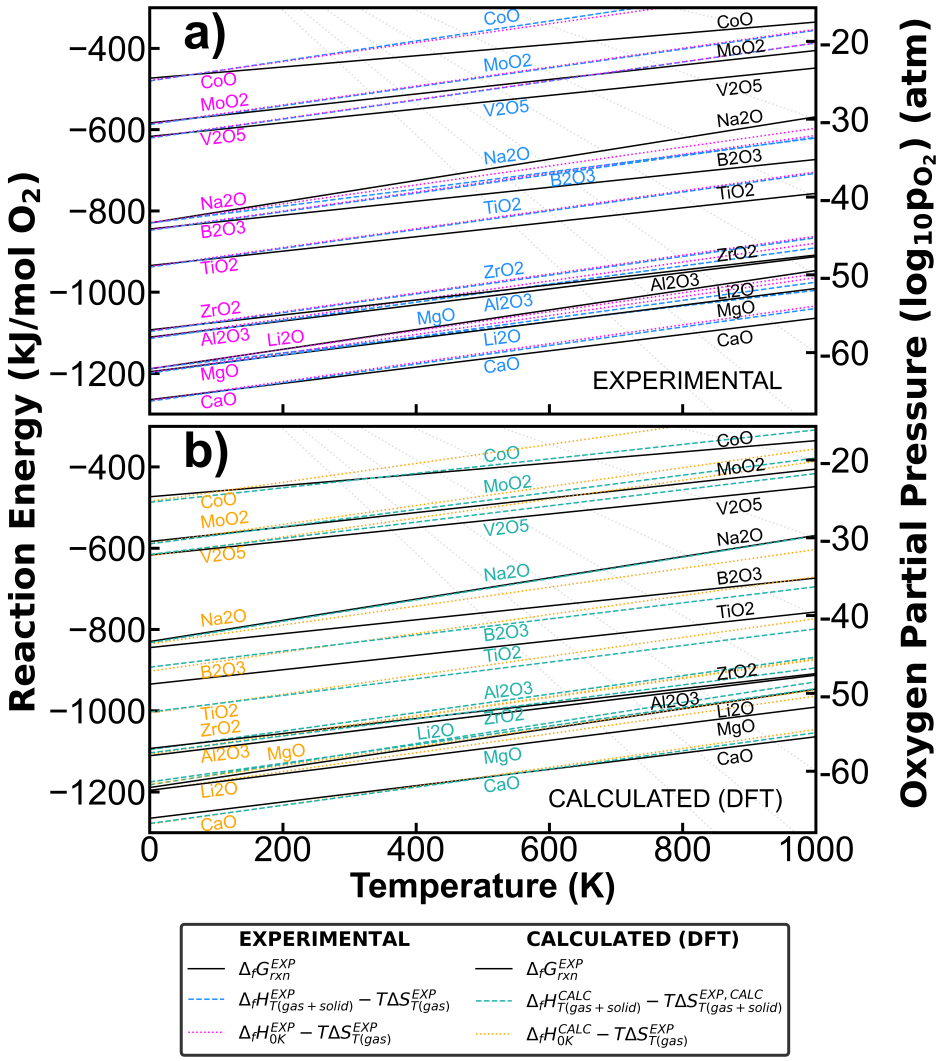

Figure 2: Ellingham diagrams for a set of binary oxides in air giving the free energy change from the $xM + \frac{y}{2}O_2 \rightarrow M_xO_y$ reaction in various models. Right y-axes show the nomographic overlay of the equilibrium oxygen partial pressure. Complimentary diagonal gray lines are drawn to show constant oxygen partial pressure at different temperatures. Enthalpies are sourced from experimental values,[28] or from MP-GGA energies. a) Reaction energies calculated with experimental free energies of formation for all elements (solid black lines), utilizing temperature dependent solid phase enthalpies but only gaseous entropy terms (dashed blue lines), and neglecting all solid phase temperature-dependence (dotted pink lines). b) Experimental reaction energies calculated with $\Delta_f G^{EXP}_T$ (solid black) overlaid with reaction free energies that incorporate MP-GGA data. Temperature dependence calculated with gas and solid phase terms included (gas-solid model) are shown with teal dashed lines. Orange dotted lines portray reaction energies calculated with the gas-only model.

For each panel in Figure 3, the reaction temperature range is shaded from red (500 °C) to blue (1,200 °C), representing a range commonly used by laboratory furnaces. Blue circles are shown for binary oxides predicted to have achievable reduction conditions under the given temperature range. Red circles, depict critical reduction chemical potentials and temperatures that are more extreme than those achievable by the furnace. Triangles similarly show reducible (blue) and not reducible (red) ternary/quaternary oxides. The left axis contains the critical effective oxygen potential ($\mu_{O,eff}$). The effective oxygen potential is calculated from the formation reaction equilibrium at a fixed gaseous atmosphere.

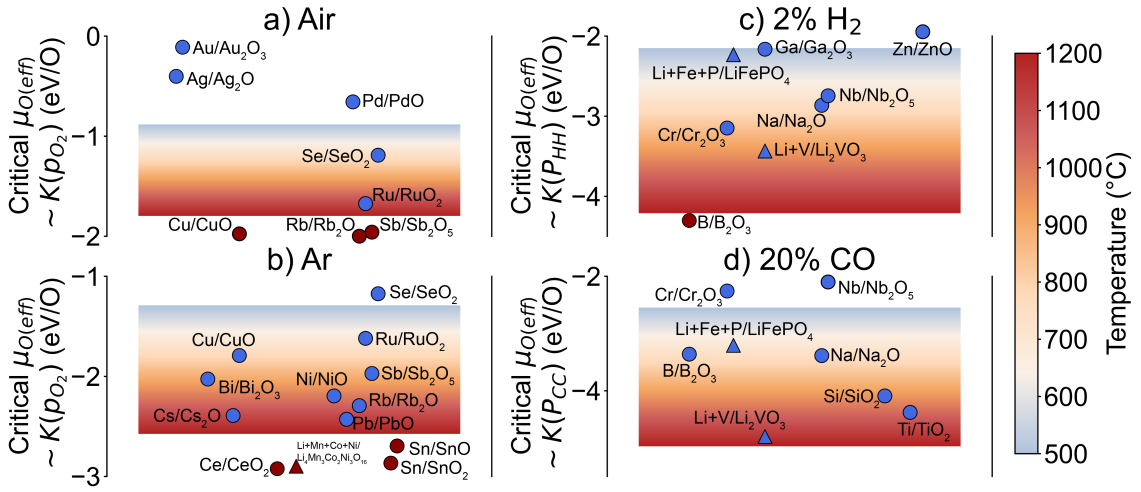

Figure 3: Overlay of the critical reduction temperature in different reducing environments calculated for binary oxides with ΔG_{rxn}^{EXP} (circles) and ternary/quaternary oxides with $\Delta G_{rxn,O_2-only}^{MP-GGA}$ (triangles). Data points indicate the effective critical oxygen chemical potential necessary to reach reduction in the fixed gas environment of (a) air (b) argon (c) argon + 2 % hydrogen (d) argon + 20% carbon monoxide. In each panel, oxides in blue are thermodynamically predicted to be reducible while oxides in red are not predicted to be reducible up to the furnace maximum temperature of 1,200 °C. The right graphs simulate H_2 and solid C reduction with H_2O:H_2 5×10^{-5} and CO_2:CO of 2.5×10^{-6}. Oxides whose reduction is calculated to occur far outside of the chemical potential range considered are not shown.

In Figure 3a showing the T and $\mu_{O,eff}$ calculated with ΔG_T^{EXP} for reduction in air, the chemical potential range accessible by the furnace is a narrow band ranging from -0.88 down to -1.80 eV/O. As such, only a handful of oxides, including silver (II) oxide, gold (III) oxide,

palladium (II), and selenium (IV) oxide are predicted to experience thermodynamically-driven reduction. In argon (Figure 3b), the range of accessible μ_O expands to -1.29 to -2.57 eV to include CuO, Bi_2O_3, Sb_2O_3, and PbO reduction. Most of the 46 binary oxides included within the collection necessitate a lower μ_O for reduction to occur.

Figure 3c depicts critical reduction temperatures in 2 % hydrogen ($P_{HH} = 5 \times 10^{-5}$). The use of hydrogen creates *effective* oxygen chemical potentials that are much lower. Therefore, though the range is modest (-2.15 to -4.21 eV/O), several materials whose reduction with air or argon is not feasible, including Li_2VO_3, V_2O_5, Na_2O and Nb_2O_5, is possible in the H_2 mixes. Al_2O_3, SiO_2, and TiO_2 are still among the oxides that cannot be reduced even with flowing 2 %H_2. However, Figure S13 shows that at a lower P_{HH} of 10^{-10}, SiO_2 and TiO_2 reduction are now thermodynamically accessible.

Reduction via 20% CO is shown in Figure 3d. The achievable $\mu_{O,eff}$ range between 500 to 1,200 °C is -2.55 to -4.97 eV/O, similar to the 2% H_2 gas. A number of oxides remain out of reach of thermodynamically driven reduction including MgO, Al_2O_3, and CaO (not pictured). Still, more oxides are predicted to be able to be reduced comparable to argon or air, including SnO_2 and Cr_2O_3 (not shown in those ranges). Lowering P_{CC} to 10^{-10} (Figure S13) enables a more extensive set of thermodynamically reducible oxides including Al_2O_3 and La_2O_3, while some oxides such as MgO remain stable against reduction.

The extremely low μ_O required for reducing oxides such as SiO_2, TiO_2, MgO, and CaO is consistent with the fact that alternative practices are used in industry to extract these metals from their oxides. Typically, these involve either starting from a less stable oxidized state, such as a chloride, or the use of sacrificial metals to increase the driving force for reduction. While metallurgical silicon can be produced from SiO_2 by carbothermal reduction at very high temperature in specialized furnaces (up to 2000 °C)[41] often the chloride route is preferred.[42] Mg is typically reduced by electrolysis from its chlorides in a molten salt electrolyte,[43] though thermal reduction with sacrificial silicon in the Pidgeon process is becoming more common.[44] Ca is usually obtained by electrochemical reduction from $CaCl_2$.[45] Titanium production is

mostly produced by reduction of $TiCl_4$[46] or through the use of Mg as a sacrificial metal.[47]

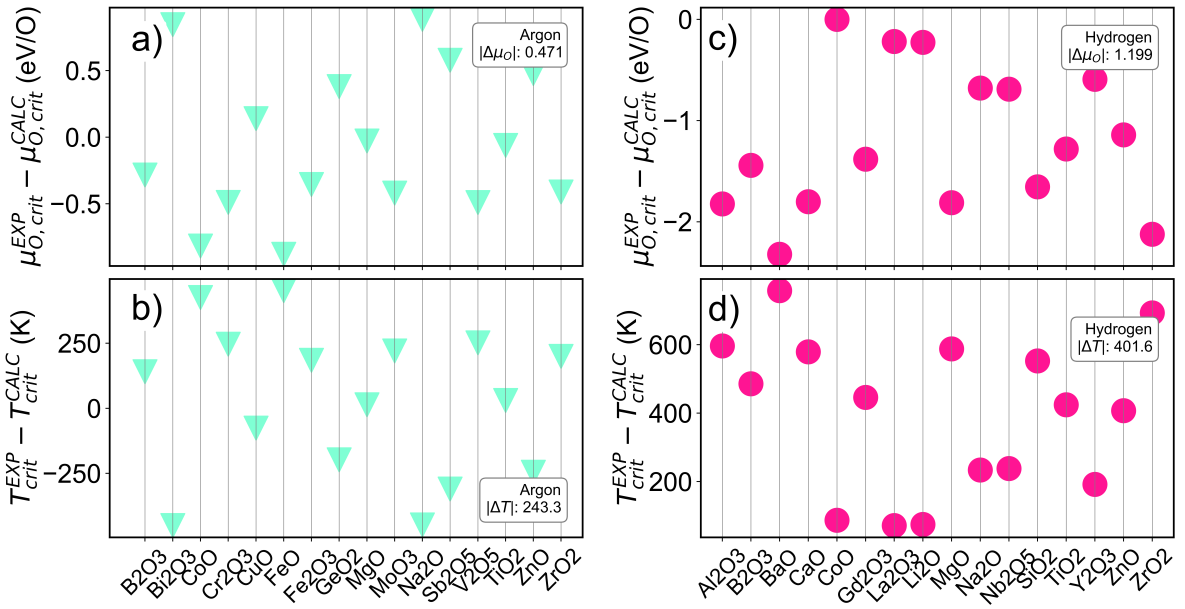

Figure 4: (a) The critical chemical potential difference $\mu^{EXP}_{O,CRIT} - \mu^{CALC}_{O,CRIT}$ and (b) critical temperature difference $T^{EXP}_{CRIT} - T^{CALC}_{CRIT}$ in argon atmosphere ($p_{O_2} = 10^{-6}$ atm) for binary oxides. (c) The critical chemical potential difference $\mu^{EXP}_{O,CRIT} - \mu^{CALC}_{O,CRIT}$ and (d) critical temperature difference $T^{EXP}_{CRIT} - T^{CALC}_{CRIT}$ in 2 % hydrogen atmosphere ($P_{HH} = 5 \times 10^{-5}$). Experimental values are calculated with entropies and enthalpies from the NIST-Janaf Thermochemical Tables and Materials Thermochemistry.[28,29] DFT-GGA 0 K enthalpies are approximated with Materials Project data fit with systematic oxidation-state and composition-dependent corrections,[32,33] and adjusted to finite temperatures without temperature effects from the solid phases (gas-only model). Oxides are chosen such that the critical reduction point occurs at temperatures where the Shomate equation is valid.

Critical Chemical Potential Errors

To characterize any errors associated with the critical μ_O introduced when GGA calculated energies are adjusted for temperature without T-contributions from the solid phases (gas-only model), we plot the critical chemical potential differences and critical temperature differences versus experimental data in argon (Figure 4a and b) and 2 % hydrogen (Figure 4c and d). $\mu^{EXP}_{O,crit} - \mu^{CALC}_{O,crit}$ for argon shows a difference of 0.471 eV/O. Critical chemical potential differences are less than 0.4 eV/O for most phases, and within 0.2 eV/O for many. Bi_2O_3

and Na_2O exhibit the largest differences of -0.846 and -0.888 eV/O, respectively. MgO has the smallest chemical potential difference in Figure 4a at 0.029 eV/O. Critical reduction temperature differences are moderate for most oxides, with all being less than 500 K. A number of oxides, such as CuO,MgO, and TiO_2, exhibit $T_{crit}^{EXP} - T_{crit}^{CALC} < 100\,°C$. Many oxide reduction temperature differences hover around 150 to 250 °C, including Cr_2O_3 (246 °C), Fe_2O_3 (184 °C), V_2O_5 (252 °C), and ZrO_2 (199 °C).

The deviations of $\mu_{O,crit}$ and T_{crit} from their values obtained with $\Delta_f G_T^{EXP}$ for hydrogen reduction (Figure 4b and d) are larger at 1.199 eV/O and 401.6 °C. The largest differences from experiment for the critical chemical potential are found in Al_2O_3 (-1.823 eV/O), BaO (-2.320 eV/O), CaO (-1.800 eV/O), MgO (-1.811 eV/O), and ZrO_2(-2.122 eV/O). These large differences lead to a calculated reduction temperature differences of 401.6 °C in 2%H_2. Among some oxides, the chemical potential and reduction temperature are much closer between MP-GGA calculated and experimental values, including for Li_2O (-0.228 eV/O; 74 °C) and La_2O_3 (-0.219 eV/O; 71 °C). Most oxides, including Gd_2O_3, B_2O_3, Na_2O, Nb_2O_5, TiO_2, Y2O3, and ZnO, exhibit differences in critical chemical potentials between about -0.5 to -2 eV/O, which leads to predicted reduction temperature differences of about 200 to 600 °C.

There are a number of different explanations for oxides with larger errors in critical chemical potential and associated predicted reduction temperatures. Similar to previous analyses, issues with enthalpies of formation from DFT persist in critical chemical potential difference calculations, including for Bi_2O_3 and Al_2O_3. In general, errors in $\mu_{O,crit}$ reflect the cumulative propagation of errors from each upstream quantity: 0 K DFT enthalpy errors, solid-phase entropy approximations, and reference state choices, all discussed in detail in the preceding sections. The material-dependence of these errors is evident in Figure 4, where TiO_2 and B_2O_3 show large deviations driven by electronic structure approximations, while CoO and Na_2O show errors consistent with neglected solid-phase entropy contributions. When enthalpy errors from total DFT energies arise, researchers may opt for specialized, system-specific DFT configurations such as in Zeng[48] to achieve higher accuracy than is provided

by high-throughput computational frameworks. For many other oxides, including CoO and Na_2O, Figure 2 demonstrates that using only gaseous O_2 to fit for temperature dependence of reaction energies is a poor approximation due to the large contribution of solid phase entropy to the reaction free energy. We anticipate the inclusion of solid phase entropies would greatly improve agreement with experiment. We note that for a few cases, such as V_2O_5[49] and Bi_2O_3,[50,51] the melting point is below the calculated reduction temperature, and thus reduction is not expected to occur (see Table S13). In total, average temperature differences for both gaseous atmospheres and air (Figure S14) are moderate, but show oxide-specific increases or decreases in deviation.

Discussion

This work introduces strategies to construct, validate, and apply thermodynamic stability models derived from DFT energies to experimental conditions. By reviewing procedures for incorporating temperature effects into DFT-GGA free energies, we evaluated their capacity to predict experimental oxidation-reduction (redox) temperatures. Our results demonstrate that at moderate temperatures, the gas-only model, utilizing 0 K GGA enthalpies and thermal corrections from O_2 gas alone, provides relatively accurate redox temperatures for most metal/oxide pairs. While incorporating solid-phase temperature effects (the gas-solid model) improves the accuracy of reaction energies and equilibrium p_{O_2}, the refinement is modest except at very high temperatures. For some specific oxides such as CoO, the large solid phase contributions to the change in entropy necessitate use of the gas-solid model even at low temperatures. To bridge the gap between theory and the laboratory, we defined critical gaseous equilibrium parameters and calculated effective oxygen chemical potentials (μ_{O_2}) that are achievable in common furnace environments (Air, argon, hydrogen, and carbon monoxide). By overlaying these potentials onto redox thresholds, we provide a thermodynamic map for key binary and ternary oxides. Ultimately, this work addresses two central challenges: (*i*

quantifying the accuracy of DFT-sourced energetic models, and *ii* calibrating computational data to real-world experimental environments.

A primary challenge in thermodynamic modeling is determining whether DFT-calculated formation energies are sufficiently accurate to describe a physical system. Deviations in formation enthalpy from 0 K DFT energies are often the largest source of error in free energies of formation. This aligns with existing literature and underscores the importance of previously published correction schemes[5–10] and functional benchmarking.[52–56] As shown in Figure 1, corrections such as those utilized within our study can bring calculated values closer to experimental data by 1 eV/O_2 or more. When oxide enthalpies are adjusted for electronic errors and zero-point energy (ZPE), the formation enthalpy of most oxides falls within ≈50 meV/O_2 of experimental values. However, these adjustments cannot be applied judiciously; specifically, when combining MP-GGA enthalpies with phonon calculations, double-counting ZPEs must be avoided as these are already included in the schemes that correct DFT enthalpies with experimental references.

While entropy is a secondary contribution at low temperatures, it governs stability in high-temperature regimes. At low temperatures, the gaseous phase entropy alone is often sufficient for calculating reaction energies (see Figure S8). The gas-solid model utilizing phonon calculations achieves high accuracy for entropies at 298 K (within ≈ 10 meV/O_2 of experiment). The necessity of including solid-phase entropy is most apparent in the improved agreement of redox reaction energies in Ellingham diagrams (Figure 2) at high temperatures. Certain oxides, such as CoO and V_2O_5, exhibit significant deviations from experimental values if solid-phase entropy is neglected. Conversely, for Group II oxides (MgO, CaO), the solid-phase contribution is negligible. We propose that the ratio of solid entropy to total entropy change ($\frac{\Delta S_{solid}}{\Delta S_{all}}$) serves as a reliable metric to justify the choice between the gas-only and gas-solid models.

We note errors in thermodynamic quantities computed with this workflow are both calculation- and material-dependent. For formation enthalpies, errors from the choice of

electronic structure method dominate for specific systems: TiO_2 and B_2O_3 show the largest deviations (Figure 1a), attributable to the absence of +U corrections and van der Waals treatments. For reaction energies and critical chemical potentials, solid-phase entropy approximations become the primary error source at elevated temperatures, particularly for CoO and Na_2O where $|\Delta S_{\text{solid}}/\Delta S_{\text{total}}|$ exceeds 20% at 298 K and grows substantially with temperature (Table S7). Additional contributions arise from the quasi-harmonic phonon approximation, Shomate equation fit uncertainties, and reference state choices embedded in the MP compatibility corrections.

By defining a "virtual furnace," we model material stability as a function of specific experimental atmospheres. We find that these models effectively produce realistic redox conditions for a diverse set of binary oxides. For instance, many oxides (Na_2O, Cr_2O_3, Nb_2O_5) require extremely low chemical potentials achievable only through H_2 or CO reducing gases Figure 3. Our predicted rankings of redox activity and reduction temperatures correspond well with experimental literature and industrial practices for carbothermal and electrochemical reduction.

Despite this broad agreement, this analysis is are sensitive to the underlying DFT energy errors. Errors in formation enthalpy and entropy propagate into $\mu_{O,crit}$ and T_{crit} variance, particularly for heavy metal oxides like Bi_2O_3 (Figure 4). Furthermore, reactions associated small entropy change from weak reducing agents can lead to large discrepancies in predicted critical temperatures (Figure S16). Nevertheless, the majority of binary oxides explored exhibited reduction temperatures within about 10% of experimental values, instilling confidence in the utility of DFT-sourced thermodynamic calculations.

Opportunities remain to refine these thermodynamic stability models. Databases of widely available DFT energies from more accurate functionals, such as r2SCAN[57] or even hybrid functionals[58] will reduce the reliance on empirical corrections, as would more complete databases of phonon calculations.[18] Extension of this framework to ternary and more complex oxide systems is a natural and valuable next step, however, this comes with added challenges,

including the scarcity of experimental thermochemical data for validation and the increasing technical difficulty and computational cost of phonon calculations for larger, lower-symmetry unit cells. More globally, thermodynamic frameworks that couple temperature, pressure, and compositional degrees of freedom will be necessary to fully leverage stability models in materials design, alongside incorporation of kinetic factors to capture the interplay between thermodynamics and kinetics in material synthesis. Configurational entropy contributions from cation disorder, relevant for complex oxides such as perovskites and spinels, also remain to be incorporated.

Conclusion

We establish key methods for creating a virtual furnace to understand phase stability within solid state synthesis. Calibration of accurate chemical potentials for solid phases and common gaseous atmospheres allows us to establish maps of reduction and oxidation accessibility for a number of key binary oxides. While limitations of this work exist for kinetic barriers and energetic modeling, we expect wide applicability of our method to solid state synthesis predictive modeling, particularly for high throughput screening work.

Acknowledgments

This work was supported by the Energy and Materials Division of the Toyota Research Institute. L.N.W. acknowledges funding support from the Bakar Institute of Digital Materials for the Planet (BIDMaP) Postdoctoral Fellowship. The authors acknowledge valuable scientific discussions with Amalie Trewartha, Steven B. Torrisi, Joseph Montoya, and Matthew J. McDermott for helping shape the project.

Supporting Information

Enthalpies of formation and empirical Shomate fit factors for gases; comprehensive enthalpy, entropy, and free energy differences including temperature dependence of reaction energies; Ellingham diagrams; compiled thermodynamic data for calculated phases and critical reduction temperatures; supplemental analysis of GGA potential, temperature differences, and thermodynamic phase competition in H_2 and CO; melting point data corresponding to manuscript Figure 4.

References

(1) Lu, Z. Computational discovery of energy materials in the era of big data and machine learning: A critical review. *Mater. Rep.: Energy* **2021**, *1*, 100047, DOI: 10.1016/j.matre.2021.100047.

(2) Aykol, M.; Montoya, J. H.; Hummelshøj, J. Rational Solid-State Synthesis Routes for Inorganic Materials. *J. Am. Chem. Soc.* **2021**, *143*, 9244–9259, DOI: 10.1021/jacs.1c04888.

(3) McDermott, M. J.; Dwaraknath, S. S.; Persson, K. A. A graph-based network for predicting chemical reaction pathways in solid-state materials synthesis. *Nat. Commun.* **2021**, *12*, DOI: 10.1038/s41467-021-23339-x.

(4) Chen, J.; Cross, S. R.; Miara, L. J.; Cho, J.-J.; Wang, Y.; Sun, W. Navigating phase diagram complexity to guide robotic inorganic materials synthesis. *Nat. Synth.* **2024**, *3*, 606—614, DOI: 10.1038/s44160-024-00502-y.

(5) Wang, L.; Maxisch, T.; Ceder, G. Oxidation energies of transition metal oxides within the GGA+U framework. *Phys. Rev. B* **2006**, *73*, DOI: 10.1103/physrevb.73.195107.

(6) Grindy, S.; Meredig, B.; Kirklin, S.; Saal, J. E.; Wolverton, C. Approaching chemical

accuracy with density functional calculations: Diatomic energy corrections. *Phys. Rev. B* **2013**, *87*, DOI: 10.1103/physrevb.87.075150.

(7) Chen, H.; Hong, Q.; Ushakov, S.; Navrotsky, A.; van de Walle, A. A simple method for computing the formation free energies of metal oxides. *Comput. Mater. Sci.* **2021**, *198*, 110692, DOI: 10.1016/j.commatsci.2021.110692.

(8) Friedrich, R.; Esters, M.; Oses, C.; Ki, S.; Brenner, M. J.; Hicks, D.; Mehl, M. J.; Toher, C.; Curtarolo, S. Automated coordination corrected enthalpies with AFLOW-CCE. *Phys. Rev. Mater.* **2021**, *5*, DOI: 10.1103/physrevmaterials.5.043803.

(9) Friedrich, R.; Usanmaz, D.; Oses, C.; Supka, A.; Fornari, M.; Buongiorno Nardelli, M.; Toher, C.; Curtarolo, S. Coordination corrected ab initio formation enthalpies. *npj Comput. Mater.* **2019**, *5*, DOI: 10.1038/s41524-019-0192-1.

(10) Friedrich, R.; Curtarolo, S. AFLOW-CCE for the thermodynamics of ionic materials. *J. Chem. Phys.* **2024**, *160*, DOI: 10.1063/5.0184917.

(11) Ong, S. P.; Wang, L.; Kang, B.; Ceder, G. Li-Fe-P-O_2 Phase Diagram from First Principles Calculations. *Chem. Mater.* **2008**, *20*, 1798–1807, DOI: 10.1021/cm702327g.

(12) Bartel, C. J.; Millican, S. L.; Deml, A. M.; Rumptz, J. R.; Tumas, W.; Weimer, A. W.; Lany, S.; Stevanović, V.; Musgrave, C. B.; Holder, A. M. Physical descriptor for the Gibbs energy of inorganic crystalline solids and temperature-dependent materials chemistry. *Nat. Commun.* **2018**, *9*, DOI: 10.1038/s41467-018-06682-4.

(13) Togo, A.; Tanaka, I. First Principles Phonon Calculations in Materials Science. *Scr. Mater.* **2015**, *108*, 1–5, DOI: 10.1016/j.scriptamat.2015.07.021.

(14) Togo, A. First-principles Phonon Calculations with Phonopy and Phono3py. *J. Phys. Soc. Jpn.* **2023**, *92*, DOI: 10.7566/jpsj.92.012001.

(15) Reuter, K.; Scheffler, M. Composition, structure, and stability of RuO2 110 as a function of oxygen pressure. *Phys. Rev. B* **2001**, *65*, DOI: 10.1103/physrevb.65.035406.

(16) Reuter, K.; Scheffler, M. First-Principles Atomistic Thermodynamics for Oxidation Catalysis: Surface Phase Diagrams and Catalytically Interesting Regions. *Phys. Rev. Lett.* **2003**, *90*, DOI: 10.1103/physrevlett.90.046103.

(17) Wang, J.-P. A Novel Process for Recovery of Key Elements from Commercial Cathode Material of End-of-Life Lithium-Ion Battery. *Archives of Metallurgy and Materials* **2021**, 745–750, DOI: 10.24425/amm.2021.136373.

(18) Jain, A.; Ong, S. P.; Hautier, G.; Chen, W.; Richards, W. D.; Dacek, S.; Cholia, S.; Gunter, D.; Skinner, D.; Ceder, G.; Persson, K. A. Commentary: The Materials Project: A materials genome approach to accelerating materials innovation. *APL Mater.* **2013**, *1*, DOI: 10.1063/1.4812323.

(19) Ong, S. P.; Richards, W. D.; Jain, A.; Hautier, G.; Kocher, M.; Cholia, S.; Gunter, D.; Chevrier, V. L.; Persson, K. A.; Ceder, G. Python Materials Genomics (pymatgen): A robust, open-source python library for materials analysis. *Comput. Mater. Sci.* **2013**, *68*, 314–319, DOI: 10.1016/j.commatsci.2012.10.028.

(20) Kresse, G.; Hafner, J. Ab initiomolecular dynamics for liquid metals. *Phys. Rev. B* **1993**, *47*, 558, DOI: 10.1103/PhysRevB.47.558.

(21) Kresse, G.; Hafner, J. Ab Initio Molecular-Dynamics Simulation of the Liquid-Metal-Amorphous-Semiconductor Transition in Germanium. *Phys. Rev. B* **1994**, *49*, 14251, DOI: 10.1103/PhysRevB.49.14251.

(22) Kresse, G.; Furthmüller, J. Efficiency of Ab-Initio Total Energy Calculations for Metals and Semiconductors Using a Plane-Wave Basis Set. *Comput. Mater. Sci.* **1996**, *6*, 15–50, DOI: 10.1016/0927-0256(96)00008-0.

(23) Kresse, G.; Furthmüller, J. Efficient Iterative Schemes for Ab Initio Total-Energy Calculations Using a Plane-Wave Basis Set. *Phys. Rev. B* **1996**, *54*, 11169–11186, DOI: 10.1103/PhysRevB.54.11169.

(24) Blöchl, P. E. Projector Augmented-Wave Method. *Phys. Rev. B* **1994**, *50*, 17953–17979, DOI: 10.1103/PhysRevB.50.17953.

(25) Kresse, G.; Joubert, D. From Ultrasoft Pseudopotentials to the Projector Augmented-Wave Method. *Phys. Rev. B* **1999**, *59*, 1758–1775, DOI: 10.1103/PhysRevB.59.1758.

(26) Perdew, J. P.; Burke, K.; Ernzerhof, M. Generalized Gradient Approximation Made Simple. *Phys. Rev. Lett.* **1996**, *77*, 3865–3868, DOI: 10.1103/physrevlett.77.3865.

(27) Jain, A.; Hautier, G.; Moore, C. J.; Ping Ong, S.; Fischer, C. C.; Mueller, T.; Persson, K. A.; Ceder, G. A high-throughput infrastructure for density functional theory calculations. *Comput. Mater. Sci.* **2011**, *50*, 2295–2310, DOI: 10.1016/j.commatsci.2011.02.023.

(28) Allison, T. JANAF Thermochemical Tables, NIST Standard Reference Database 13. 1998; http://kinetics.nist.gov/janaf/.

(29) O. Kubaschewski, P. J. S., C. B. Alcock *Materials Thermochemistry*, 6th ed.; Pergamon Press: New York, 1993.

(30) Shomate, C. H. A Method for Evaluating and Correlating Thermodynamic Da ta. *J. Phys. Chem.* **1954**, *58*, 368–372, DOI: 10.1021/j150514a018.

(31) Huang, L.-F.; Rondinelli, J. M. Electrochemical phase diagrams for Ti oxides from density functional calculations. *Phys. Rev. B* **2015**, *92*, DOI: 10.1103/physrevb.92.245126.

(32) Wang, A.; Kingsbury, R.; McDermott, M.; Horton, M.; Jain, A.; Ong, S. P.; Dwaraknath, S.; Persson, K. A. A framework for quantifying uncertainty in DFT energy corrections. *Sci. Rep.* **2021**, *11*, DOI: 10.1038/s41598-021-94550-5.

(33) Jain, A.; Hautier, G.; Ong, S. P.; Moore, C. J.; Fischer, C. C.; Persson, K. A.; Ceder, G. Formation enthalpies by mixing GGA and GGA+U calculations. *Phys. Rev. B* **2011**, *84*, DOI: 10.1103/physrevb.84.045115.

(34) Li, D.; Tang, Q.; He, J.; Li, B.; Ding, G.; Feng, C.; Zhou, H.; Zhang, G. From Two- to Three-Dimensional van der Waals Layered Structures of Boron Crystals: An Ab Initio Study. *ACS Omega* **2019**, *4*, 8015–8021, DOI: 10.1021/acsomega.9b00534.

(35) Park, K.; Raman, M.; Olatunbosun, A.-J.; Pohlmann, J. Revisiting DFT+U calculations of TiO2 and the effect of the local-projection size. *AIP Adv.* **2024**, *14*, DOI: 10.1063/5.0211720.

(36) Samat, M. H.; Taib, M. F. M.; Jaafar, N. K.; Hassan, O. H.; Yahya, M. Z. A.; Ali, A. M. M. First-principles studies on phase stability of TiO2 by using GGA+U calculations. AIP Conference Proceedings. 2018; p 020058, DOI: 10.1063/1.5066699.

(37) Matsumoto, N.; Watanabe, T.; Kato, K. Impurity analyses of high-purity carbon monoxide gas using micro gas chromatography for development as a certified reference material. *J. Chromatogr. A* **2013**, *1282*, 190–193, DOI: 10.1016/j.chroma.2013.01.089.

(38) Ellingham, H. J. T. Reducibility of oxides and sulphides in metallurgical processes. *J. Soc. Chem. Ind.* **1944**, *63*, 125–160, DOI: 10.1002/jctb.5000630501.

(39) Shang, S.-L.; Lin, S.; Gao, M. C.; Schlom, D. G.; Liu, Z.-K. Ellingham diagrams of binary oxides. *APL Mater.* **2024**, *12*, DOI: 10.1063/5.0216426.

(40) Pralong, V.; Gopal, V.; Caignaert, V.; Duffort, V.; Raveau, B. Lithium-Rich Rock-Salt=Type Vanadate as Energy Storage Cathode: $Li_{2-x}VO_3$. *Chem. Mater.* **2011**, *24*, 12–14, DOI: 10.1021/cm203281q.

(41) Du, H.; Chen, Y.; Wang, Y.; Wang, H.; Guo, X.; Zhang, Z.; Li, H.; Xing, P.; Zhuang, Y. Thermodynamic mechanism of metallurgical-grade silicon preparation

from silica fume by carbothermal reduction. *J. Clean. Prod.* **2025**, *529*, 146817, DOI: 10.1016/j.jclepro.2025.146817.

(42) Chen, J. M.; Chang, F. W.; Chang, C. Y. Chlorination kinetics of silicon dioxide in the presence of carbon. *Ind. Eng. Chem. Res.* **1990**, *29*, 778–783, DOI: 10.1021/ie00101a011.

(43) Demirci, G.; Karakaya, I. *Magnesium Technology 2012*; Springer International Publishing, 2012; pp 59–62, DOI: 10.1007/978-3-319-48203-3_11.

(44) Wu, L.; Han, F.; Liu, G. *Comprehensive Utilization of Magnesium Slag by Pidgeon Process*; Springer Singapore, 2021; pp 45–68, DOI: 10.1007/978-981-16-2171-0_2.

(45) Zaikov, Y. P.; Batukhtin, V. P.; Shurov, N. I.; Ivanovskii, L. E.; Suzdaltsev, A. V. Calcium Production by the Electrolysis of Molten CaCl2—Part I. Interaction of Calcium and Copper-Calcium Alloy with Electrolyte. *Metall. Mater. Trans. B* **2013**, *45*, 961–967, DOI: 10.1007/s11663-013-9990-x.

(46) Okabe, T. H.; Takeda, O. *Extractive Metallurgy of Titanium*; Elsevier, 2020; pp 65–95, DOI: 10.1016/b978-0-12-817200-1.00005-3.

(47) PANG, J.; KONG, L.-x.; ZHU, L.-g.; XU, B.-q.; XU, J.-j.; BAI, C.-l.; YANG, B. Preparation of ultralow-oxygen titanium by direct reduction of TiO2. *Trans. Nonferrous Met. Soc. China* **2024**, *34*, 681–693, DOI: 10.1016/s1003-6326(23)66427-1.

(48) Zeng, Z.; Chan, M. K. Y.; Zhao, Z.-J.; Kubal, J.; Fan, D.; Greeley, J. Towards First Principles-Based Prediction of Highly Accurate Electrochemical Pourbaix Diagrams. *J. Phys. Chem. C* **2015**, *119*, 18177–18187, DOI: 10.1021/acs.jpcc.5b03169.

(49) Emhjellen, L. K.; Haugsrud, R. Oxygen Exchange Across the Melting Point of V_2O_5—Advancing Beyond Solids? *Adv. Funct. Mater.* **2025**, *35*, 2501274, DOI: 10.1002/adfm.202501274.

(50) Levin, E. M.; Roth, R. S. Polymorphism of Bismuth Sesquioxide. I. Pure Bi_2O_3. *J. Res. Natl. Bur. Stand. Sect. A* **1964**, *68A*, 189–195, DOI: 10.6028/jres.068A.019.

(51) Klinkova, L. A.; Nikolaichik, V. I.; Barkovskii, N. V. Thermal Stability of Bi_2O_3. *Russ. J. Inorg. Chem.* **2007**, *52*, 1822–1829, DOI: 10.1134/S0036023607120030.

(52) Goerigk, L.; Grimme, S. A thorough benchmark of density functional methods for general main group thermochemistry, kinetics, and noncovalent interactions. *Phys, Chem. Chem. Phys.* **2011**, *13*, 6670, DOI: 10.1039/c0cp02984j.

(53) Mohn, C. E.; Fjellvåg, H.; Vajeeston, P.; Valldor, M.; Bergum, K. Benchmarking Density Functional Theory for Accurate Calculation of Nitride Band Gaps. *J. Chem. Theory and Comput.* **2026**, DOI: 10.1021/acs.jctc.5c01703.

(54) Karton, A.; de Oliveira, M. T. Good Practices in Database Generation for Benchmarking Density Functional Theory. *WIREs Comput. Mol. Sci.* **2025**, *15*, DOI: 10.1002/wcms.1737.

(55) Sure, R.; Grimme, S. Comprehensive Benchmark of Association (Free) Energies of Realistic Host–Guest Complexes. *J. Chem. Theory Comput.* **2015**, *11*, 3785–3801, DOI: 10.1021/acs.jctc.5b00296.

(56) Marques, E. A.; De Gendt, S.; Pourtois, G.; van Setten, M. J. Benchmarking First-Principles Reaction Equilibrium Composition Prediction. *Molecules* **2023**, *28*, 3649, DOI: 10.3390/molecules28093649.

(57) Furness, J. W.; Kaplan, A. D.; Ning, J.; Perdew, J. P.; Sun, J. Accurate and Numerically Efficient r2SCAN Meta-Generalized Gradient Approximation. *J. Phys. Chem. Lett.* **2020**, *11*, 8208–8215, DOI: 10.1021/acs.jpclett.0c02405.

(58) Krukau, A. V.; Vydrov, O. A.; Izmaylov, A. F.; Scuseria, G. E. Influence of the exchange

screening parameter on the performance of screened hybrid functionals. *J. Chem. Phys.* **2006**, *125*, 224106, DOI: 10.1063/1.2404663.

TOC Graphic

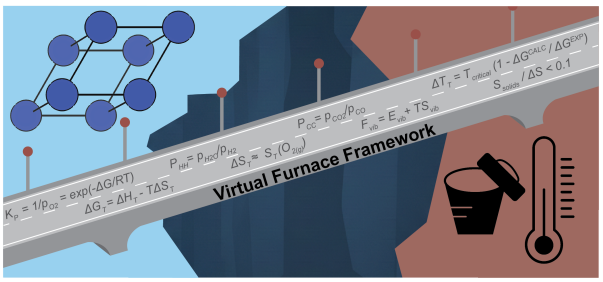
$K_p = 1/p_{O2} = \exp(-\Delta G/RT)$
$\Delta G_T = \Delta H_T - T\Delta S_T$
$P_{H2} = P_{H2O}/p_{H2}$
$\Delta S_T = S_T(O_{2(g)})$
$P_{CO} = P_{CO2}/p_{CO}$
$F_{vib} = E_{vib} + TS_{vib}$
$\Delta T_T = T_{critical}(1 - \Delta G^{CALC} / \Delta G^{EXP})$
$S_{yields} / \Delta S < 0.1$
Virtual Furnace Framework